This is a preprint, the final version is subject to change, of the American Mineralogist (MSA)
Cite as Authors (Year) Title. American Mineralogist, in press.
DOI: https://doi.org/10.2138/am-2020-6901

Revision 2

Seismic detectability of carbonates in the deep Earth: a Nuclear Inelastic Scattering study

Stella Chariton[1], Catherine McCammon[1], Denis M. Vasiukov[2], Michal Stekiel[3], Anastasia Kantor[1,4], Valerio Cerantola[4], Ilya Kupenko[5], Timofey Fedotenko[2], Egor Koemets[1], Michael Hanfland[4], Alexandr I. Chumakov[4] and Leonid Dubrovinsky[1]

[1] Bayerisches Geoinstitut, Universität Bayreuth, 95440 Bayreuth, Germany
[2] Laboratory of Crystallography, Universität Bayreuth, 95440 Bayreuth, Germany
[3] Institute of Geosciences, Goethe Universität, 60438 Frankfurt am Main, Germany
[4] ESRF, The European Synchrotron, CS40220, 38043 Grenoble Cedex 9, France
[5] Institute for Mineralogy, Universität Münster, 48149 Münster, Germany

ABSTRACT

Carbonates play an important role in the transport and storage of carbon in the Earth's mantle. However, the abundance of carbon and carbonates in subduction zones is still an unknown quantity. In order to understand which are the most abundant accessory phases and how they influence the dynamical processes that operate within the Earth, investigations on the vibrational, elastic and thermodynamic properties of these phases are crucial for interpreting the seismological observations. Recently, the Nuclear Inelastic Scattering (NIS) method has proved to be a useful tool to access information on the lattice dynamics, as well as to determine Debye sound velocities of Fe-bearing materials. Here we derive the acoustic velocities from two carbonate compositions in the $FeCO_3$-$MgCO_3$ binary system up to ~ 70 GPa using the NIS method. We conclude that more Mg-rich samples, in this case $(Fe_{0.26}Mg_{0.74})CO_3$, have ~ 19 %

higher sound velocities than the pure end-member Fe composition. In addition, we observed a significant velocity increase after the Fe^{2+} spin transition was complete. After laser heating of $FeCO_3$ at lower mantle conditions, we observed a dramatic velocity drop, which is probably associated with thermal decomposition to another phase. Parallel to our NIS experiments, we conducted a single crystal X-ray diffraction (SCXRD) study to derive the equation of states of $FeCO_3$ and $(Fe_{0.26}Mg_{0.74})CO_3$. The combined information from NIS (i.e. Debye velocities) and SCXRD (i.e. densities and bulk moduli) experiments enabled us to derive the primary and shear wave velocities of our samples. Our results are consistent with results obtained by other methods in previous studies, including Brillouin spectroscopy, inelastic X-ray scattering and DFT calculations, supporting NIS as a reliable alternative method for studying the elastic properties of Fe-bearing systems at high pressures and temperatures. Finally, we discuss the seismic detectability of carbonates. We determine that nearly 22 wt% of CO_2 must be present in the subduction slab in order to detect a 1 % shear wave velocity decrease compared to non-carbonated lithologies at transition zone to lower mantle boundary depths.

Keywords: Nuclear Inelastic Scattering; Fe-bearing carbonates; High pressure and temperature; spin transition; elastic wave velocities

1. INTRODUCTION

Over the past two decades, carbonates have been suspected to be one of the main carbon carriers into the Earth's deep interior (Dasgupta and Hirschman 2010). Rare, but indisputable, examples of natural samples in the form of superdeep-diamond inclusions (Kaminsky et al. 2012), exhumed metamorphic rocks and xenoliths (Becker and Altherr 1992; Liu et al. 2015) or

carbonate-rich lavas (Fischer et al. 2009) have supported this hypothesis. Samples that carry a mantle signature are extremely rare and thus an experimental approach has been used to investigate such systems. More concretely, the physical properties of various carbonate minerals have been extensively studied at pressures and temperatures of the Earth's mantle to determine their structural and chemical stability at these great depths (e.g. Isshiki et al. 2004; Merlini et al. 2012; Cerantola et al. 2017).

Recent experimental studies on the elastic properties of carbonates at extreme conditions raise questions on whether deep carbon cycling can be detected using seismic methods. Sanchez-Valle et al. (2005) first studied carbonated lithologies (eclogites, peridotites) at ambient conditions with results suggesting that their velocity contrast with non-carbonated mantle may be below the threshold of present seismic resolution unless an unrealistically high carbonate fraction is present. However, it was predicted that under high pressure and particularly through the Fe^{2+} spin crossover, the elastic wave velocities of carbonates will increase substantially (Shi et al. 2008). Later Fu et al. (2017) reported the primary and shear wave velocities of a natural Fe-bearing magnesite crystal at high pressure (70 GPa) with emphasis on the abnormal elasticity that it presents across the Fe spin transition. Finally, Stekiel et al. (2017) investigated the effect of composition in the binary system $FeCO_3$-$MgCO_3$ on the elastic stiffness coefficients including through the spin transition. All previous studies concluded that carbonates have a strong anisotropic behavior. Nonetheless, they also demonstrated that different velocities can be obtained using different techniques.

Several methods can be used to determine elastic wave velocities. Ultrasonic measurements are a reliable method, but they are mainly restricted to upper mantle conditions (< 25 GPa). Brillouin spectroscopy has traditionally been used for obtaining accurate velocities at a

much wider pressure range (< 100 GPa) using a diamond anvil cell. However, *in situ* high pressure and temperature experiments are challenging, the method is restricted by the sample quality, since non-transparent samples cannot be measured and often the diamond signal blocks the sample signal at very high pressures. The latter problem can be overcome by the combination of Brillouin light scattering (BLS) and the impulsive stimulated light scattering (ISS) techniques. IXS is another technique that enables measurement of sound velocities of opaque samples. Sound velocities can be measured along selected directions in the crystal, but the determination of mean velocity can require more time compared to other methods. Computational methods, such as density functional theory (DFT) calculations, are an interesting alternative, but have their own challenges. They require a careful choice of various input parameters and produce results that need to be confirmed experimentally (Winkler and Milman, 2014).

Nuclear inelastic scattering (NIS) is a technique that provides information on the thermoelastic properties of a material by probing lattice vibrations (Chumakov and Rüffer 1998). It is most common to measure the partial density of phonon states (pDOS) of materials using NIS. However, the relationship between the low-energy regime of a reduced DOS (i.e. rDOS = pDOS/Energy^2) function and the Debye sound velocity of the sample was soon recognized (Hu et al. 2003). Since then, NIS has been used to derive accurate Debye velocities from monoatomic solids (Hu et al. 2003) to diatomic solids and solid solution systems (Sturhahn and Jackson 2007; Sinmyo et al. 2014) at ambient conditions. The method was successfully used in high-pressure environments using diamond anvil cells (McCammon et al. 2016; Vasiukov et al. 2018) and also at high temperatures (Shen et al. 2004; Kupenko et al. 2015).

In this work, we use NIS to determine *in-situ* the sound velocities of Fe-bearing carbonates at pressure and temperature conditions of the Earth's mantle. Siderite ($FeCO_3$) and

ferromagnesite (Fe,Mg)CO_3 are polyatomic compounds with strong anisotropic behavior, owing to their calcite-type structure ($R\bar{3}c$). We present a parallel high-pressure compressibility study using single-crystal X-ray diffraction (SCXRD) which enables us to derive secondary (Vs) and primary (Vp) wave velocities from the calculated Debye velocities using NIS. The ultimate goal of our study is to investigate the possibility to detect carbonates using the present seismic technology and provide further insight into the Earth's deep carbon cycle.

2. METHODS

2.1. Sample preparation and NIS measurements

Synthetic samples were prepared in either powder or single crystal form. All Fe-bearing samples were enriched in the ^{57}Fe isotope, in order to enhance the NIS signal and decrease the collection time. Cerantola et al. (2015) described the synthesis procedure in detail, especially for the Fe end-member ($FeCO_3$). Further synthesis of solid solutions in the binary system $FeCO_3$-$MgCO_3$ was carried out with an additional multi anvil experiment. $^{57}FeCO_3$ and $MgCO_3$ powders were well mixed in stoichiometric proportions and placed into a Re capsule. Crystals of 10 – 80 μm in size were obtained after 10 min annealing at 1550 (±50) ºC and 18 GPa. We collected NIS spectra from two different compositions, namely $^{57}FeCO_3$ and $MgCO_3$ with 26 mol% ^{57}Fe. The chemical composition of our samples was determined after structure solution and refinements using the SCXRD method. Our ferromagnesite crystals obtained by multi anvil synthesis had varying compositions with average 26 mol% (± 4 mol%) Fe content.

NIS spectra were collected at the Nuclear Resonance beamline, ID18 (Rüffer and Chumakov, 1996), at the European Synchrotron Radiation Facility (ESRF, Grenoble, France) during timing mode (16-Bunch or Hybrid storage ring mode). High pressure was generated by panoramic diamond anvil cells (pDACs) (Fig. 1), while high temperature was obtained using a

double-sided laser heating system, available at ID18 (Kupenko et al. 2012; Aprilis et al. 2017). The use of a beryllium gasket was necessary since the NIS signal is measured perpendicular to the incident beam direction (Fig. 1). Powder samples were loaded inside the pDACs either with KCl as pressure-transmitting medium or with paraffin oil (Table S1). Single crystal samples (~20x15 μm^2, length x thickness) were loaded mostly with paraffin oil. Only a small minority of samples were loaded with Ar gas under pressure (Kurnosov et al. 2008). We recognize the limited hydrostatic conditions that paraffin oil and halides offer during cold compression compared to noble gases, but gas loading was often unsuccessful due to the large instability of beryllium gaskets. Pressure was determined using ruby fluorescence spectra before and after each NIS measurement. Depending on the degree of hydrostatic conditions of each measurement, different calibration references were used (Dewaele et al. 2008; Mao et al. 1986).

The energy dependencies of NIS were collected over a large energy range around the ^{57}Fe nuclear resonance energy of 14.4 keV. We used the range -20 to 100 meV for collections at ambient temperature and the range -100 to 100 meV for collections during heating (Fig. 2). For the majority of our NIS measurements we used a high-resolution monochromator with 2 meV energy bandwidth. The finest energy bandwidth of 0.5 meV was used only for a few sample collections due to limited beamtime. The collection time of one NIS spectrum varied from approximately 15 to 40 min. For each pressure point several scans (3-12) were collected in order to increase statistics and minimize artefacts due to instrument instability. Typically, samples at higher pressures (>50 GPa) required collection of more scans due to the increased background. The experimental set-up at ID18 allowed us to collect nuclear forward scattering spectra (NFS) in parallel with the NIS signal. We used the NFS spectra to distinguish between pressure points where Fe^{2+} was in the high spin (HS) state (Fig. 3a) and the low spin (LS) state (Fig. 3b).

2.2 Calculation of velocities

The partial DOS and rDOS functions were derived from the initial NIS spectra according to software developed by Kohn and Chumakov (2000). Then, the Debye sound velocities (V_D) were calculated according to the "homogeneous model" as described by Sinmyo et al. (2014) and the following equation (Achterhold et al. 2002; Hu et al. 2003):

$$D(E) = \frac{\tilde{m}}{m} \cdot \frac{E^2}{2\pi^2\hbar^3 n V_D} \quad , \qquad (1)$$

where $\tilde{m}$ is the mass of the nuclear resonant isotope (i.e. ^{57}Fe), m is the average atomic mass, $\hbar$ is Planck's constant and n is the density of atoms. Only the low energy regime of the rDOS function, typically an interval of 5meV between the energy range 2-10 meV, is used for the determination of the V_D velocities. For each pressure point, we selected the appropriate 5 meV energy range judging from the statistics of the measurement and the energy bandwidth of the high resolution monochromator that was used. Finally, using the relationship between $V_D$velocities and the primary and shear wave velocities, the latter can be calculated by solving the following three equations:

$$\frac{3}{V_D^3} = \frac{1}{V_P^3} + \frac{2}{V_S^3} \qquad (2)$$

$$V_P = \sqrt{\frac{K + \frac{4}{3}G}{\rho}} \qquad (3)$$

$$V_S = \sqrt{\frac{G}{\rho}} \quad , \qquad (4)$$

where K is the adiabatic bulk modulus, G is the shear modulus and ρ is the density.

2.2 Single crystal X-ray Diffraction

In order to determine velocities, it was necessary to obtain accurate ρ and K values of the same sample compositions that we used for NIS experiments. This was possible by obtaining the equations of state (EoS) of $FeCO_3$ and $(Fe_{0.26}Mg_{0.74})CO_3$ up to ~66 and 60 GPa, respectively. Two single crystals of each composition were separately loaded inside two BX-90 cells (Kantor et al. 2012) with Boehler-Almax design diamonds and equivalent WC seats. The diamond culet size was 250 μm diameter. We used Re gaskets and Ne as the pressure transmitting medium, where neon under pressure served as a pressure determinant (Fei et al. 2007) (http://kantor.50webs.com/diffraction.htm).

The SCXRD study was carried out at the high-pressure X-ray diffraction beamline, ID15b, at ESRF. We collected XRD patterns during ± 38º omega rotation, with 1 sec exposure time for every 0.5º step. Integration of the reflection intensities and absorption corrections was performed using CrysAlis^{PRO} software (Rigaku OD 2015). The software package JANA (Petricek et al. 2014) was used for structure solution and refinements. When the number of reflections was sufficiently high, all atoms were refined in the anisotropic approximation, giving in total 10 refinable parameters for typically 80-90 unique reflections with $F_o > 3\sigma (F_o)$. In the few datasets that the reflection to refined parameter ratio was too low, we refined only the anisotropic parameters of the metal cations (Fe, Mg). We used the software package EoSFit7 (Angel et al. 2014; Gonzalez-Platas et al. 2016) to determine equations of state that incorporated weighted fits for both pressure and volume.

3. RESULTS

3.1. Equations of state

The pressure-induced spin transition of Fe^{2+} in Fe-bearing carbonates has been documented by several methods, including Mössbauer spectroscopy (Cerantola et al. 2015), X-ray diffraction (Lavina et al. 2010a), X-ray Raman scattering (Weis et al. 2017), and Raman spectroscopy (Müller et al. 2016). There is much discussion in the literature concerning the exact pressure that the spin transition takes place, whether it is sharp or not, and how impurity elements in a natural sample affect the transition. Despite the arguments, most of the previous studies agree that the spin transition in $FeCO_3$ starts around 40-44 GPa, while the onset of the transition can shift to slightly higher pressures with the addition of Mg. In this study, we detected the spin transition by NIS, NFS and SCXRD on synthetic samples.

Using SCXRD we observed a dramatic volume drop of ~10% above ~44 GPa for $FeCO_3$ (Fig. 4) as a previous study has suggested (Lavina et al. 2010a). At approximately the same pressure, a less dramatic volumetric effect (~ 3%) was seen in the solid solution $(Fe_{0.26}Mg_{0.74})CO_3$ (Fig. 4). These observations are directly associated with the spin crossover of Fe^{2+}, which induces a reduction of the metal cation radius and thus a volume collapse of FeO_6 octahedra (Fig. S1). At the same time, the rigid triangular CO_3 units slightly expand (Fig. S2).

In the case of $FeCO_3$ with HS Fe^{2+} (i.e. pressure interval 0 – 44 GPa), the volume data were fitted to both a 2nd and 3rd order Birch-Murnaghan (BM) equation of state, resulting in K_0=122.0(6) GPa , K_0'= 4, V_0= 292.66(2) Å^3 and K_0=125(3) GPa, K_0'= 3.8(2), V_0= 292.66(2) Å^3, respectively. The 2nd order BM equation gives a statistically better fit to our data, and K_0' does not differ significantly from 4. These values are in relatively good agreement with previous studies (Lavina et al. 2010a, Zhang et al. 1998) (Table S2). For $(Fe_{0.26}Mg_{0.74})CO_3$ with HS Fe^{2+} (i.e. pressure interval 0 – 44 GPa), a 2nd order BM-EoS was used resulting in K_0=115.1(5) GPa , K_0'= 4 and V_0= 282.69(8) Å^3. Alternatively, the parameters become K_0=112(1) GPa and K_0'=

206 4.3(1) if a 3rd order BM-EoS is used. In Figure 4 we compare the EoS of the two samples when
207 K_0'=4.We observe that at 44 GPa, pure $FeCO_3$ (K_{44GPa}=284.2(6) GPa, V_{44GPa}=232.2(2) Å^3) is less
208 compressible than the $(Mg_{0.74}Fe_{0.26})CO_3$ (K_{44GPa}=273.4(5) GPa, V_{44GPa}=223.0(2) Å^3) by ~4%.

209 Fitting the P-V data after spin crossover to an EoS involves greater uncertainties. Since
210 the K_0' parameter of the above equations of states (i.e. HS-Fe^{2+}) is close to 4, we decided to fit a
211 2nd order BM EoS for both compositions with LS-Fe^{2+} (Fig. 4). Thus, for LS-siderite (i.e.
212 pressure interval 46 – 66 GPa) the zero pressure volume and bulk modulus become V_0= 250(1)
213 Å^3 and K_0= 172(8) GPa, respectively. In the case of LS-ferromagnesite (i.e. pressure interval 48
214 – 60 GPa), we obtain V_0= 266(4) Å^3 and K_0= 146(13) GPa. We note that at 48 GPa, pure siderite
215 (K_{48GPa}= 346(8) GPa, V_{48GPa}=207.0(2) Å^3) becomes even less compressible than Fe-bearing
216 $MgCO_3$ (K_{48GPa}= 314(13) GPa, V_{48GPa}=216.0(2) Å^3) by ~10%.

217

218 **3.2. Sound Velocities**

219 3.2.1 Cold compression

220 There are two primary effects detected by NIS in this study. First is the effect of chemical
221 composition on the sound velocities. Equation 1 demonstrates that the Debye velocity of a
222 material is inversely related to its density (via the n parameter). Note that we obtained the
223 density of our two carbonate samples as a function of pressure using SCXRD (Table S1). In
224 addition, V_D velocities are inversely related to both the curvature of the pDOS at low energies (<
225 10 meV) and the intercept of the rDOS at zero energy (Hu et al. 2003). For example, Figure 5a
226 illustrates the rDOS functions obtained for our two samples at ambient conditions. We observe
227 that $(Mg_{0.74}Fe_{0.26})CO_3$ shows clearly a lower zero energy intercept compared to $FeCO_3$, leading
228 to the result that $(Mg_{0.74}Fe_{0.26})CO_3$ has a ~19% higher sound velocity than pure $FeCO_3$ (Fig. 3c).

The second effect relates to the influence of the Fe^{2+} spin transition on sound velocities. After Fe^{2+} adopts a LS electronic configuration, the V_D velocities increase substantially. For example, Figure 5b demonstrates the pDOS functions of $FeCO_3$ with increasing pressure and along the spin transition. Note that for HS-$FeCO_3$, the pDOS curvature decreases with increasing pressure (35 to 44 GPa) (Fig. 5b), and thus the V_D velocities constantly increase (Fig. 3c). However, above 50 GPa the pDOS curvatures are significantly lowered, resulting in substantially higher (by nearly 19%) V_D velocities. We observe similar but less pronounced behavior (~9%) in the case of $(Mg_{0.74}Fe_{0.26})CO_3$ (Fig. 3c).

We collected NIS data from both powders and single crystals. The crystals were placed in the sample chamber without selecting specific crystallographic orientations. At the same pressure conditions, each crystal gave different pDOS functions and thus different sound velocities outside of experimental error. For example, the V_D velocities of two siderite crystals at ~2.5 GPa differ by ~6% (Fig. 3c; Table S1). Another notable example is the V_D velocities of a single crystal $(Mg_{0.74}Fe_{0.26})CO_3$ and its powdered form, which at 1 bar differ by ~5% (Fig. 3c; Table S1). NIS is sensitive to crystallographic orientation (Chumakov and Rüffer 1998). Similar effects have been previously reported for a $FeBO_3$ single crystal (Chumakov et al. 1997; Parlinski et al. 2001), which is isostructural to the calcite-type carbonates. The different velocities that we observe are likely related to the strong anisotropic nature of carbonates. This interesting phenomenon will be the subject of more careful investigation in the future.

3.2.2. During and after heating

The capability for *in situ* high pressure and high temperature collection is one of the great advantages of the NIS method. Previous studies have demonstrated the feasibility of such

experiments in laser-heated diamond anvil cells (e.g. Shen et al. 2004). In particular, the double-sided laser set-up installed at the ID18 beamline is able to provide a stable laser beam and operate in a continuous or pulsed mode for heating periods as long as ~12 h (Kupenko et al. 2012; Aprilis et al. 2017).

The sample temperature during heating is firstly determined by the thermal radiation signal using spectroradiometry. Additionally, we determine the temperature from the Boltzmann factor using the NIS signal (Chumakov et al. 1996; Shen et al. 2004). For example, Figure 2 shows three NIS spectra of the same sample with increasing temperature. The peak around +16 meV represents phonon creation, while the peak at -16 meV corresponds to phonon annihilation. As temperature increases, the intensity of the two peaks becomes more symmetric and their ratio is given by the Boltzmann factor, which has an exponential relation to the sample temperature (see supplementary material, Eq. S3). Nearly all temperatures shown in Table S3 were calculated from the combination of the two methods. Temperatures below 1000 K could be estimated only from the NIS signal.

We observed that laser heating of siderite at conditions close to the top of the lower mantle decreases the sound velocities slightly (Fig. 3c). Such a result is consistent with the changes of thermal parameters expected when increasing the temperature of the sample (e.g. Yang et al. 2014). However, due to the limited number of data points we cannot provide more definitive results on the temperature dependence of velocities. The slight velocity decrease that we observed is consistent for all data within measurement uncertainty in nearly all cases, except for one point at ~26 GPa (Fig. 3c; Table S3). We postulate that the pressure in the cell dropped from ~37.0(5) to 26(2) GPa during laser heating (~1700 K), because the ruby signal showed non-hydrostatic conditions and one of the diamonds anvils was found to be cracked. Although the

lower velocity of this sample might be the result of a pressure gradient, it could also be an indication of a change such as due to a decomposition reaction. Therefore, we consider this measurement to be uncertain.

Heating at lower mantle conditions (>1200 km depth) resulted in an abrupt velocity drop (Fig. 3c). It is likely that the NIS signal collected is not from the original sample which may have thermally decomposed. We were not able to collect XRD patterns of the sample; however, an extensive study on the phase stability of synthetic pure $FeCO_3$ (Cerantola et al. 2017) showed that siderite decomposes to high-pressure Fe_3O_4 (Bbmm) close to the P-T conditions of our measurements. To our knowledge, there are no data in the literature that describe the elasticity of magnetite at pressures above ~20 GPa, so we are not able to compare the velocities we obtained at 56-60 GPa and 900-1700 K (Table S3). Our hypothesis that siderite decomposition is responsible for the observed velocity decrease does not rule out other possible interpretations of our data. However we have excluded the possibility of a pressure drop in the cell and/or the presence of mixed spin states in the sample (Fig. S4).

4. Discussion

It is possible to estimate the primary and secondary elastic wave velocities using NIS (Eq. 2), even though NIS is not able to retrieve a sample full elastic tensor of the sample. To calculate velocities, it is crucial to have accurate values of the sample density and bulk modulus as a function of pressure. In the present study, we have obtained ρ and K_P (K at pressure) (Table S1) as well as V_D using SCXRD and NIS, respectively. Substitution of equations (3) and (4) in (2) results in equation (5) where G, the shear modulus, is the only unknown parameter:

$$\frac{3}{V_D^3} - \left(\frac{K}{\rho} + \frac{4G}{3\rho}\right)^{-\frac{3}{2}} - 2\left(\frac{G}{\rho}\right)^{-\frac{3}{2}} = 0 \quad . \qquad (5)$$

We extract the shear modulus by solving equation (5), where the uncertainty in G is estimated through error propagation. Knowing all the necessary parameters, we were able to determine V_P and V_S through equations (3) and (4) (Table S1).

Figure 6 illustrates the elastic wave velocities of $FeCO_3$ and $(Mg_{0.74}Fe_{0.26})CO_3$ determined from our NIS experiments. For comparison, we have plotted the velocity curves derived from fits to experimental IXS data combined with DFT calculations reported by Stekiel et al. (2017). Although our velocities are slightly lower than those from the DFT calculations, we observe that the two datasets follow similar trends (Fig. 6). In particular, the agreement between studies at ambient conditions is remarkable (Sanchez-Valle et al. 2011; Stekiel et al. 2017). The discrepancies at high pressure may be due to several reasons as presented below.

The bulk modulus is important to the calculation of elastic wave velocities, but the uncertainty in K_P is not high enough to explain the discrepancies. For example, the error of ±8 GPa at low spin $FeCO_3$ will induce less than 1% difference in the V_P and V_S calculation. However, Kantor et al. (2008) demonstrated that bulk moduli values obtained for the same sample by XRD and IXS methods may differ up to 20 %. Such an inconsistency may explain why our velocities, with K determined by XRD, are lower than those reported by Stekiel et al. (2017), where K was determined by IXS and DFT calculations (Fig. S3). In order to consider this further, we compared the Debye velocities obtained from the two studies (Fig. 3c). The calculation of V_D using NIS does not depend on the bulk modulus (Eq. 1). Indeed, the two datasets are in good agreement with the exception of LS-$FeCO_3$, where we observed an ~11% mismatch. Previous studies showed that the velocity jump after the Fe^{2+} spin transition is most pronounced for Fe-rich compositions (Stekiel et al. 2017; Fu et al. 2017). Although, our data

follow this trend with increasing Fe content, the case of the pure Fe end-member remains unexplained.

Sinmyo et al. (2014) discussed in detail other reasons for discrepancies between NIS results and other methods, such as the minor effect of impurities and defects or the more considerable effect of Fe clustering in synthetic samples. In Figure 6, we note that V_P velocities obtained by NIS have higher discrepancies with previous studies compared to our V_S values. This is an expected pattern. Primary and secondary velocities in this study are calculated using V_D; however around 90% of the V_D value comes from V_S (Eq. 2). Our estimations of V_S are hence better determined from NIS than those of V_P. Finally, we note that differences may be due to the strongly anisotropic nature of carbonates. Sturhahn and Jackson (2007) showed that the equations used for the estimation of V_P and V_S using NIS hold only approximately for anisotropic materials and the resulting velocities may deviate from actual values by a few percent or more for strongly anisotropic materials.

5. Implications

Previous studies have considered the possibility to detect carbonates in the deep Earth using geophysical methods. Sanchez-Valle et al. (2014) suggested that, depending on composition, an unrealistically high CO_2 content (~15-20 wt%) must be present in order to observe a contrast above the assumed 2% seismic resolution limit between carbonates and crust lithologies. Similarly, Yang et al. (2014) concluded a low probability of detecting ferromagnesian carbonates in the upper mantle where more than 10 wt% pure $MgCO_3$ (~5 wt% CO_2) would be needed to produce a 1% velocity drop. On the other hand, Fu et al. (2017) argued that at lower mantle depths (~1200 km) where the Fe^{2+} spin crossover takes place, the abnormal

elastic behavior of Fe-bearing carbonates would induce a drastic decrease of V_P (~10%), thus increasing the probability to seismically detect such a feature. Stekiel et al. (2017) did not observe this abnormal elasticity, likely due to the coarser pressure steps in their experiments and that calculations were performed for pure spin states. However they concluded that the Fe spin transition would induce an observable velocity contrast (~1% Vs decrease) if at least 8-9% $(Fe_{0.15}\ Mg_{0.85})CO_3$ were present in pyrolitic mantle. Here we elaborate further on the seismic detectability of Fe-bearing carbonates based on the effects of composition, spin transition, and phase stability at Earth's mantle conditions.

Due to the limited constraint on V_P from our NIS measurements as explained above, we consider only V_S for our data comparisons to the PREM model (Dziewonski and Anderson 1981). The AK135 reference model, which differs mostly for upper mantle velocities compared to PREM, could be used instead (Kennett et al. 1995); however our conclusions are not substantially changed. We acknowledge that the use of averaged one-dimensional models (i.e. PREM, AK135) likely sets an upper limit for carbonate detectability, since 2D and 3D models with higher resolution in subduction regions will provide more sensitivity. Modern seismic techniques can offer high-resolution velocity perturbation maps with a scale as fine as 1 % (e.g. Fukao and Obayashi 2013; Chen et al. 2017).

Previous studies agree that the most realistic ferromagnesian carbonate composition expected in deep subducted slabs has approximately ~15 wt% Fe content (McDonough and Sun 1995; Dasgupta et al. 2004). Thus, using our data (see also Eq. S4-S7 in the supplementary material and details therein) and assuming a linear relation we calculated the shear velocities of $(Fe_{0.15}Mg_{0.85})CO_3$ at room temperatures (Fig. 7). Subsequently, we determined the minimum amount of $(Fe_x\ Mg_{x-1})CO_3$ (where x=1, 0.26 or 0.15) needed to detect carbonates by geophysical

methods. Therefore, we estimated the amount of carbonate necessary to induce a 1% shear velocity drop at various depths within the Earth (Table S4). For example, at uppermost upper mantle depths (~300 km), carbonates of $(Mg_{0.85}Fe_{0.15})CO_3$ composition would be unlikely to be detected (Fig. 7). On the other hand, at the same depths the presence of 4 wt% $FeCO_3$ would be enough to cause a 1% shear velocity decrease. However, the latter scenario is unrealistic since the average composition of subducted carbonates is mostly dolomitic (i.e. Ca- and Mg-rich). Note that as we move to greater depths Ca is preferentially partitioned into silicates and thus Fe-bearing magnesite becomes the dominant carbonate composition that is subducted to the deep Earth (Biellmann et al. 1993).

Based on a realistic scenario, our calculations (Table S4) indicate that 9 wt% $(Mg_{0.85}Fe_{0.15})CO_3$ would be required to detect carbonates in the lowermost part of the transition zone (~600 km). The presence of 5 wt% $(Fe_{0.15}Mg_{0.85})CO_3$ well mixed with a lower mantle assemblage will be sufficient to detect carbonates in the uppermost lower mantle (~1000 km). The Fe spin transition that follows at greater depths (~1450 km) would, in contrast, increase the amount of $(Mg_{0.85}Fe_{0.15})CO_3$ (~6 wt%) needed to detect a 1 % V_S drop. Nevertheless, the latter case may be questionable, since the effect of temperature was not considered so far.

In the present study, we demonstrated that the elastic wave velocities of $FeCO_3$ during heating at low pressures are very close to those of the original sample before the thermal treatment (Fig. 3c). On the other hand, at high pressures and after the spin transition, there is a high probability that $FeCO_3$ will decompose (Cerantola et al. 2017) and thus velocities will dramatically drop. Therefore, if we take into consideration the effect of temperature in the above calculations, then the presence of Fe-oxides may play an important role in the velocity profiles of the lower mantle compared to carbonates. This interesting observation motivates further work.

Although, $FeCO_3$ appears thermodynamically unstable at lower mantle conditions, the addition of Mg can extend its chemical and structural stability to greater depths (Ishiiki et al. 2004; Cerantola et al. 2017). Hence, any assessment of the amount of $(Fe_{0.15}\ Mg_{0.85})CO_3$ needed to produce a 1 % velocity drop at low- spin-state-related depths (>1200 km) will strongly depend on its stability at these conditions.

We have discussed the complications of detecting carbonates at middle lower mantle (>1200 km) and uppermost upper mantle (< 410 km) depths, but detecting carbonates in the transition zone (410 to 660 km) may be challenging as well, due to competition from other phases that could also cause velocity anomalies. Many candidates have been proposed to cause anisotropic anomalies at these depths, such as hydrous wadsleyite, ringwoodite, akimotoite, and other dense hydrous magnesium silicate phases (Nowacki et al. 2015; Buchen et al. 2018). Nonetheless, owing to their high anisotropy and velocity contrast compared to major mantle mineral assemblages, carbonates are equally plausible candidates.

Further geological aspects are important to consider regarding carbonates. Our calculations demand the presence of at least 9 wt% $(Fe_{0.15}\ Mg_{0.85})CO_3$ at ~600 km, which means that sediments and the subducted oceanic lithosphere should have at least ~4.4 wt% CO_2 content initially. This is a significant amount of CO_2 that most present-day subduction zones do not have. In addition, a large portion of subducted CO_2 will recycle to the crust or atmosphere mainly via volcanic activities. A precise estimate of CO_2 net flux has been a challenging task and strongly depends on the local geologic setting (Dasgupta and Hirschmann 2010; Kelemen and Manning 2015). Therefore, if we assume that only 20 % of subducted CO_2 will be stored in the deep convecting mantle, this would imply that the initial subducted material would need to contain ~22 wt% CO_2 in order to detect carbonates at the transition zone – lower mantle boundary.

412 A few subduction trenches exist today that contain a high amount of CO_2 (Plank and
413 Langmuir 1998), such as the Guatemala (DSDP site 495), Peru (IODP site 321) and Colombian
414 (DSDP site 504) trenches. Interestingly, the subduction zone under Guatemala is a well-known
415 example where a slab deeply penetrates the lower mantle and is associated with either the
416 subduction of the Cocos plate or with remnants of the Farallon plate (Fukao and Obayashi 2013).
417 Likewise, the Nazca plate subducts under Peru and Colombia with a north-east inclination and
418 the slab is known to penetrate the 660 discontinuity and be trapped in the uppermost lower
419 mantle (Fukao and Obayashi 2013). These are some of the regions that are of high interest for
420 possible future geophysical surveys looking for carbonates in the deep Earth.

421 There are other influencing parameters that could be considered. For example, the
422 anisotropic behavior of carbonates could affect the threshold limit of carbonate detection as
423 described above. However, this strongly depends on the existence of lattice preferred orientation
424 (LPO) and/or foliation of carbonates, a topic which is poorly examined in the literature so far. In
425 addition, the formation of isolated carbonate-rich reservoirs could give rise to anisotropic
426 anomalies in the mantle. This scenario is highly plausible due to the low solubility of carbon in
427 silicates and the large immiscibility gap between carbonate and silicate melts (Shcheka et al.
428 2006). Finally, our discussion of carbonate detection is based on present-day carbonate
429 sedimentation rates and plate tectonic activity. However, carbon incorporation in the mantle
430 could have been quite different in the past. These are important topics to be considered, and
431 while they are beyond the scope of the present study, they help to motivate future work in this
432 area.

433

434 **Acknowledgements**

We thank the European Synchrotron Radiation Facility for provision of synchrotron radiation (ID18, ID15b). The project was supported by funds from the German Science Foundation (DFG) through the CarboPaT Research Unit FOR2125 (Mc3/20, Du393/9) and the German Federal Ministry for Education (BMBF).

REFERENCES

Achterhold, K., Keppler, C., Ostermann, A., van Bürck, U., Sturhahn, W., Alp, E.E., and Parak, F.G. (2002) Vibrational dynamics of myoglobin determined by the phonon-assisted Mössbauer effect. Physical Review E, 65, 051916.

Rigaku Oxford Diffraction (2015) CrysAlis^{PRO} software system, version 1.171, Rigaku corporation, Oxford, UK.

Angel, J.R., Alvaro, M., and Gonzalez-Platas, J. (2014) EosFit7c and a Fortran module (library) for equation of state calculations. Zeitschrift für Kristallographie – Crystalline Matters 229, 405–419.

Aprilis, C., Strohm, C., Kupenko, I., Linhardt, S., Laskin, A., Vasiukov, D.M., Cerantola, C., Koemets, E.G., McCammon, C., Kurnosov, A., and others (2017) Portable double-sided pulsed laser heating system for time-resolved geoscience and materials science applications. Review of Scientific Instruments, 88, 084501.

Becker, H., and Altherr, R. (1992) Evidence from ultra-high pressure marbles for recycling of sediments into the mantle. Nature, 358, 745-748.

Biellmann, C., Gillet, P., Guyot, F., Peyronneau, J., and Reynard, B. (1993) Experimental evidence for carbonate stability in the Earth's lower mantle. Earth and Planetary Science Letters, 118, 31-41.

458 Buchen, J., Marquardt, H., Speziale, S., Kawazoe, T., Boffa-Ballaran, T., and Kurnosov, A.
459 (2018) High-pressure single-crystal elasticity of wadsleyite and the seismic signature of
460 water in the shallow transition zone. Earth and Planetary Science Letters, 498, 77-87.
461 Cerantola, V., McCammon, C., Kupenko, I., Kantor, I., Marini, C., Wilke, M., Ismailova, L.,
462 Solopova, N., Chumakov, A.I., Pascarelli, S., and others (2015) High-pressure
463 spectroscopic study of siderite ($FeCO_3$) with focus on spin crossover. American
464 Mineralogist, 100, 2670-2681.
465 Cerantola, V., Bykova, E., Kupenko, I., Merlini, M., Ismailova, L., McCammon, C., Bykov,
466 M., Chumakov, A.I., Petitgirard, S., Kantor, I., and others (2017) Stability of iron-bearing
467 carbonates in the deep Earth's interior. Nature Communications, 8, 15960.
468 Chen, C., Zhao, D., Tian, Y., Wu, S., Hasegawa, A., Lei, J., Park, J-H., and Kang, I-B. (2017)
469 Mantle transition zone, stagnant slab and intraplate volcanism in Northeast Asia.
470 Geophysical Journal International, 209, 68-85.
471 Chumakov, A.I., Rüffer, R., Baron, A.Q.R, Grünsteudel, H., and Grünsteudel, H.F. (1996)
472 Temperature dependence of nuclear inelastic absorption of synchrotron radiation in a-^{57}Fe.
473 Physical Review B, 44, R9599.
474 Chumakov, A.I., Rüffer, R., Baron, A.Q.R., Grünsteudel, H., Grünsteudel, H.F., and Kohn,
475 V.G. (1997) Anisotropic inelastic nuclear absorption. Physical Review B, 56, 10758.
476 Chumakov, A.I., and Rüffer, R. (1998) Nuclear inelastic scattering. Hyperfine Interactions,
477 113, 59-79.
478 Dasgupta, R., Hirschmann, M.M., and Withers, A.C. (2004), Deep global cycling of carbon
479 constrained by solidus of anhydrous, carbonated eclogite under upper mantle conditions,
480 Earth and Planetary Science Letters, 227, 73–85.

Dasgupta, R., and Hirschmann, M.M. (2010) The deep carbon cycle and melting in Earth's interior. Earth and Planetary Science Letters, 298, 1-13.

Dewaele, A., Datchi, F., Loubeyre, P., and Mezouar, M. (2008) High pressure–high temperature equations of state of neon and diamond. Physical Review B, 77, 094106.

Dziewonski, A.M., and Anderson, D.L. (1981) Preliminary reference Earth model. Physics of the Earth and Planetary Interiors, 25, 297-356.

Fei, Y., Ricolleau, A., Frank, M., Mibe, K., Shen, G., and Prakapenka, V. (2007) Toward an internally consistent pressure scale. Proceedings of the National Academy of Sciences, 104, 9182–9186.

Fischer, T.P., Burnard, P., Marty, B., Hilton, D.R., Füri, E., Palhol, F., Sharp, Z.D., and Mangasini, F. (2009) Upper-mantle volatile chemistry at Oldoinyo Lengai volcano and the origin of carbonatites. Nature Letters, 459, 07977.

Fu, S., Yang, J, and Lin, J-F. (2017) Abnormal elasticity of single-crystal magnesiosiderite across the spin transition in Earth's lower mantle. Physical Review Letters, 118, 036402.

Fukao, Y., and Obayashi, M. (2013) Subducted slabs stagnant above, penetrating through, and trapped below the 660 km discontinuity. Journal of Geophysical Research: Solid Earth, 118, 5920-5938.

Gonzalez-Platas, J., Alvaro, M., Nestola, F., and Angel, R.J. (2016) EosFit7-GUI: A new GUI tool for equation of state calculations, analyses and teaching. Journal of Applied Crystallography, 49, 1377-1382.

Hu, M.Y., Sturhahn, W., Toellner, T.S., Mannheim, P.D., Brown, D.E., Zhao, J., and Alp, E.E. (2003) Measuring velocity of sound with nuclear resonant inelastic x-ray scattering. Physical Review B, 67, 094304.

Isshiki, M., Irifune, T., Hirose, K., Ono, S., Ohishi, Y., Watanuki, T., Nishibori E., Takata, M., and Sakata, M. (2004) Stability of magnesite and its high-pressure form in the lowermost mantle. Nature, 427, 60-63.

Kaminsky, F. (2012) Mineralogy of the lower mantle: A review of 'super-deep' mineral inclusions in diamond. Earth-Science Reviews, 110, 127-147.

Kantor, A., Kantor, I., Kurnosov, A., Dubrovinsky, L., Krisch, M., Bossak, A., and Jacobsen, S. (2008) Anelasticity of Fe_xO at high pressure. Applied Physics Letters, 93, 034106.

Kantor, I., Prakapenka, V., Kantor, A., Dera, P., Kurnosov, A., Sinogeikin, S., Dubrovinskaia, N., and Dubrovinsky, L. (2012) BX90: A new diamond anvil cell design for X-ray diffraction and optical measurements. Review of Scientific Instruments, 83, 125102.

Kelemen, P.B., and Manning, C.E. (2015) Reevaluating carbon fluxes in subduction zones, what goes down, mostly comes up. Proceedings of the National Academy of Sciences, 112, 3997-4006.

Kennett, B.L.N., Engdahl, E.R., and Buland, R. (1995) Constraints on seismic velocities in the earth from travel times Geophysical Journal International, 122, 108-124.

Kohn, V.G., and Chumakov, A.I. (2000) DOS: Evaluation of phonon density of states from nuclear resonant inelastic absorption. Hyperfine Interactions, 125, 205-221.

Kupenko, I., Dubrovinsky, L., Dubrovinskaia, N., McCammon, C., Glazyrin, K., Bykova, E., Boffa-Ballaran, T., Sinmyo, R., Chumakov, A., Potapkin, V., and others (2012): Portable double-sided laser-heating system for Mo̧ssbauer spectroscopy and X-ray diffraction experiments at synchrotron facilities with diamond anvil cells. Review of Scientific Instruments, 83, 124501.

526 Kupenko, I., Strohm, C., McCammon, C., Cerantola, V., Glazyrin, K., Petitgirard, S.,
527 Vasiukov, D., Aprilis, G., Chumakov, A.I., Rüffer, R., and L. Dubrovinsky (2015)
528 differentiated nuclear resonance spectroscopy coupled with pulsed laser heating in
529 diamond anvil cells. Review of Scientific Instruments, 86, 114501.
530 Kurnosov, A., Kantor, I., Boffa-Ballaran, T., Lindhardt, S., Dubrovisnky, L., Kuznetsov, A.,
531 and Zehnder, B.H. (2008) A novel gas-loading system for mechanically closing of various
532 types of diamond anvil cells. Review of Scientific Instruments, 79, 045110.
533 Lavina, B., Dera, P., Downs, R.T., Yang, W., Sinogeikin, S., Meng, Y., Shenand, and G.,
534 Schiferl, D. (2010a) Structure of siderite $FeCO_3$ to 56 GPa and hysteresis of its spin-
535 pairing transition. Physical Review B, 82, 064110.
536 Lavina, B., Dera, P., Downs, R.T., Tschauner, O., Yang, W., Shebanova, O., and Shen, G.
537 (2010b) Effect of dilution on the spin pairing transition in rhombohedral carbonates. High
538 Pressure Research, 30, 224-229.
539 Liu, Y., He, D., Gao, C., Foley, S., Gao, S., Hu, Z., Zong, K., and Chen, H. (2015) First direct
540 evidence of sedimentary carbonate recycling in subduction-related xenoliths. Scientific
541 Reports, 11547.
542 Mao, H.K., Xu, J., and Bell, P.M. (1986) Calibration of the ruby pressure Gauge to 800 kbar
543 under quasi-hydrostatic conditions. Journal of Geophysical Research, 91, 4673-7676.
544 McCammon, C., Caracas, R., Glazyrin, K., Potapkin, V., Kantor, A., Sinmyo, R., Prescher, C.,
545 Kupenko, I., Chumakov, A.I., and Dubrovinsky, L. (2016) Sound velocities of bridgmanite
546 from density of states determined by nuclear inelastic scattering and first-principles
547 calculations. Progress in Earth and Planetary Science, doi:10.1186/s40645-016-0089-2.

McDonough, W.F., and Sun, S.S. (1995) The composition of the Earth. Chemical Geology, 120, 223-253.

Merlini, M., Crichton, W.A., Hanfland, M., Gemmi, M., Müller, H., Kupenko, I., and Dubrovinsky, L. (2012) Structures of dolomite at ultrahigh pressure and their influence on the deep carbon cycle. Proceedings of the National Academy of Sciences, 109, 13509-13514.

Müller, J., Speziale, S., Efthimiopoulos, I., Jahn, S., and Koch-Müller, M. (2016) Raman spectroscopy of siderite at high pressure: Evidence for a sharp spin transition. American Mineralogy, 101, 2638–2644.

Nowacki, A., Kendall, J-M., Wookey, J., and Pemberton, A. (2015) Mid-mantle anisotropy in subduction zones and deep water transport. Geochemistry Geophysics Geosystems, 16, 764–784.

Parlinski, K., Lażewski, J., Jochym, P.T., Chumakov, A., Rüffer, R., and Kresse, G. (2001) Influence of magnetic interaction on lattice dynamics of $FeBO_3$. Europhysics Letters, 56, 275-281.

Petricek, V., Dusek, M., and Palatinus, L. (2014) Crystallographic Computing System JANA2006: General features. Zeitschrift für Kristallographie - Crystalline Materials, 229, 345–352.

Plank, T., and Langmuir, C.H. (1998) The chemical composition of subducting sediment and its consequences for the crust and mantle. Chemical Geology, 145, 325–394.

Rüffer, R., and Chumakov, A.I. (1996) Nuclear Resonance Beamline at ESRF. Hyperfine Interactions, 97/98, 589-604.

570 Sanchez-Valle, C., Ghosh, S., and Rosa, A.D. (2011) Sound velocities of ferromagnesian
571 carbonates and the seismic detection of carbonates in eclogites and the mantle.
572 Geophysical Research Letters, 38, L24315.
573 Shcheka, S., Wiedenbeck, M., Frost, D.J., and Keppler, H. (2006) Carbon solubility in mantle
574 minerals. Earth and Planetary Science Letters, 245, 730-742.
575 Shen, G., Sturhahn, W., Alp, E.E., Zhao, J., Toellner, T.S., Prakapenka, V.B., Meng, Y., and
576 Mao, H-R. (2004) Phonon density of states in iron at high pressures and high temperatures.
577 Physics and Chemistry of Minerals, 31, 353-359.
578 Shi, H., Luo, W., Johansson, B., and Ahuja, R. (2008) First-principles calculations of the
579 electronic structure and pressure-induced magnetic transition in siderite $FeCO_3$. Physical
580 Review B, 78, 155119.
581 Sinmyo, R., Glazyrin, K., McCammon, C., Kupenko, I., Kantor, I., Potapkin, V., Chumakov,
582 A.I., Rüffer, R., and Dubrovinsky, L. (2014) The influence of solid solution on elastic
583 wave velocity determination in (Mg,Fe)O using nuclear inelastic scattering. Physics of the
584 Earth and Planetary Interiors, 229, 16-23.
585 Stekiel, M., Nguyen-Thanh, T., Chariton, S., McCammon, C., Bosak, A., Morgenroth, W.,
586 Milman, V., Refson, K., and Winkler, B. (2017) High pressure elasticity of $FeCO_3$-$MgCO_3$
587 carbonates. Physics of the Earth and Planetary Interiors, 271, 57-63.
588 Sturhahn, W., and Jackson J.M. (2007) Geophysical applications of nuclear resonant
589 spectroscopy. Geological Society of America, 421, 157-174.
590 Vasiukov, D.M., Ismailova, L., Kupenko, I., Cerantola, V., Sinmyo, R., Glazyrin, K.,
591 McCammon, C., Chumakov, A.I., Dubrovinsky, L., and Dubrovinskaia, N. (2018) Sound

592 velocities of skiagite–iron–majorite solid solution to 56 GPa probed by nuclear inelastic
593 scattering. Physics and Chemistry of Minerals, 45, 397-404.
594 Weis, C., Sternemann, C., Cerantola, V., Sahle, C.J., Spiekermann, G., Harder, M., Forov, Y.,
595 Kononov, A., Sakrowski, R., Yavas, H., and others (2017) Pressure driven spin transition
596 in siderite and magnesiosiderite single crystals. Scientific Reports, 7, 16526.
597 Winkler, B., and Milman, V. (2014) Density functional theory based calculations for high
598 pressure research. Zeitschrift für Kristallographie, 229, 112–122.
599 Yang, J., Mao, Z., Lin, J-F., and Prakapenka, V.B. (2014) Single-crystal elasticity of the deep-
600 mantle magnesite at high pressure and temperature. Earth and Planetary Science Letters,
601 392, 292–299.
602 Zhang, J., Martinez, I., Guyot, F., and Reeder, R.J. (1998) Effects of Mg-Fe^{2+} substitution in
603 calcite-structure carbonates: Thermoelastic properties. American Mineralogist 83, 280-287.
604

List of Figure Captions

Figure 1: Schematic representation of the panoramic diamond anvil cell (pDAC) created using AutoDesk Fusion 360 (user interactive version: https://a360.co/2NE8RJw). The geometry of the incident beam and NIS and NFS signals are indicated.

Figure 2: Example of NIS spectra collected from a $FeCO_3$ sample at high pressure and various temperature conditions. The total collection time of each spectrum is ~5 hrs. The shaded grey area indicates the elastic peak that is subtracted during data processing.

Figure 3: Representative nuclear forward scattering (NFS) spectra for **a)** Fe^{2+} high spin state (<44 GPa) and **b)** Fe^{2+} low spin state (>50 GPa). **c)** Debye sound velocities of siderite and Fe-bearing magnesite with increasing pressure. Triangles refer to powder samples, while circles indicate single crystal samples with random crystallographic orientation. Our data are compared to previously reported DFT calculations (Stekiel et al. 2017) and show good agreement between studies.

Figure 4: Equations of state (EoS) of single crystal $FeCO_3$ and $(Mg_{0.74}Fe_{0.26})CO_3$. The error bars fall within the size of the symbols.

Figure 5: a) Reduced density of state (rDOS) functions of $FeCO_3$ and $(Mg_{0.74}Fe_{0.26})CO_3$ at ambient pressure, demonstrating the effect of composition on the sound velocities. The arrow points at the data points (blue lines) that are considered for the calculation of V_D using Equation 1. The lower intercept of the rDOS curve at zero energy indicates higher velocities. **b)** Partial density of state (pDOS) functions of $FeCO_3$ along the spin transition. The lower curvature of the pDOS curve at low energies (< 10 mev) indicates higher velocities. Note the abrupt peak shifts once the transition is completed.

627 **Figure 6:** Pressure dependence of the primary (V_P) and secondary (V_S) wave velocities of our
628 two carbonate compositions as derived from the Debye velocities. The errors bars shown are
629 estimated using error propagation (see supplemental information). Our data show similar
630 trends to previous studies. The grey shaded area indicates the Fe^{2+} low spin state.

631 **Figure 7:** Shear wave velocities (V_S) of the PREM model compared to our modeled carbonate
632 compositions as a function of depth (see also Table S4). The effect of temperature is not taken
633 into account in this plot (see text for details).

Figure 1

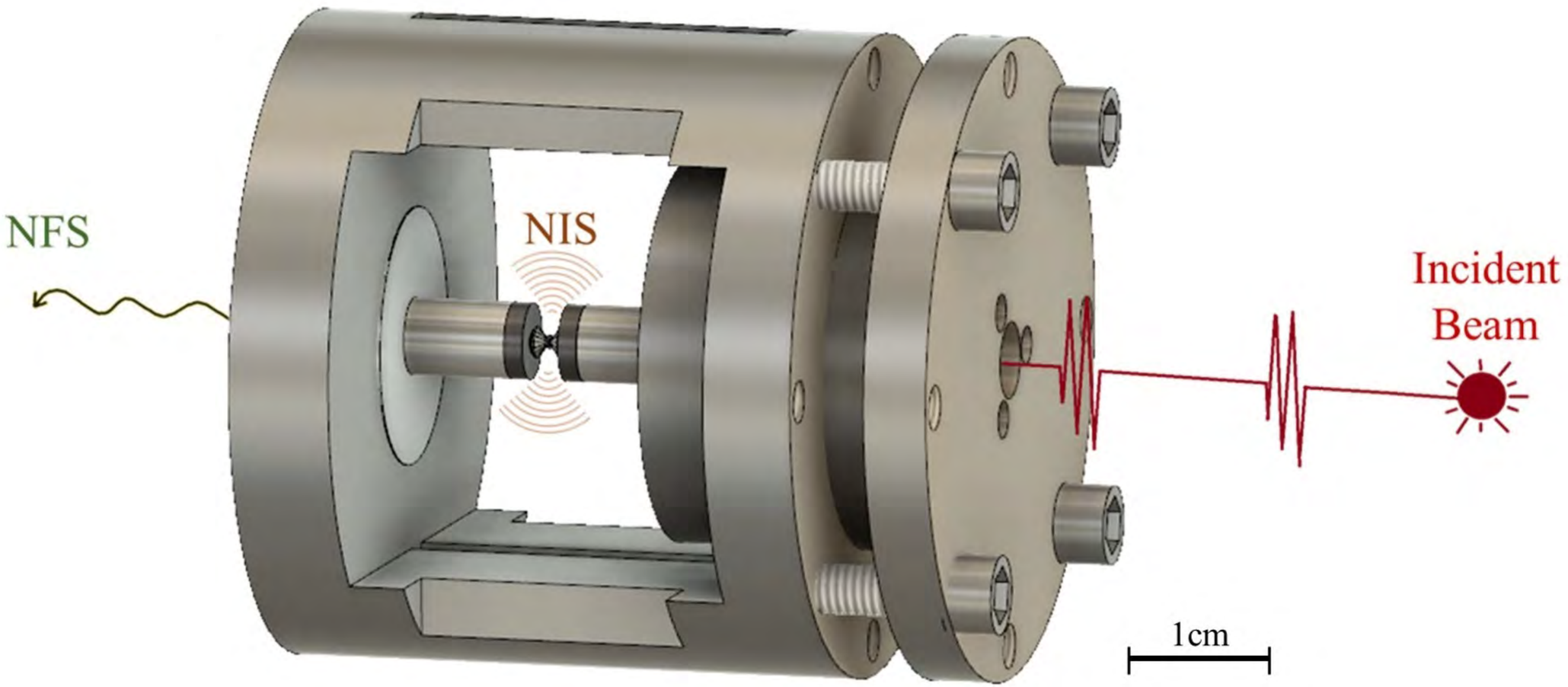

Figure 2

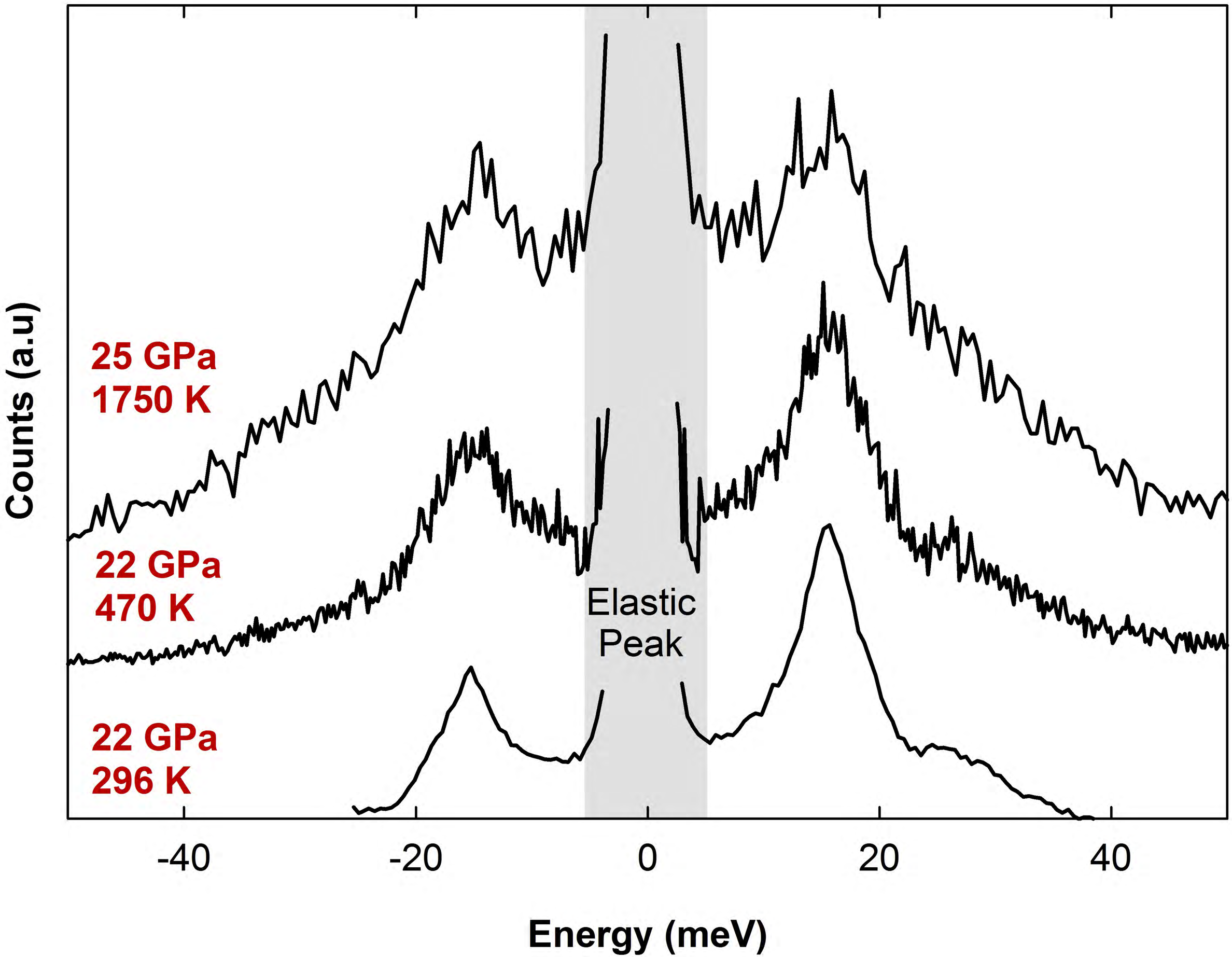
Counts (a.u)
25 GPa
1750 K
22 GPa
470 K
22 GPa
296 K
Elastic
Peak
-40
-20
0
20
40
Energy (meV)

Figure 3

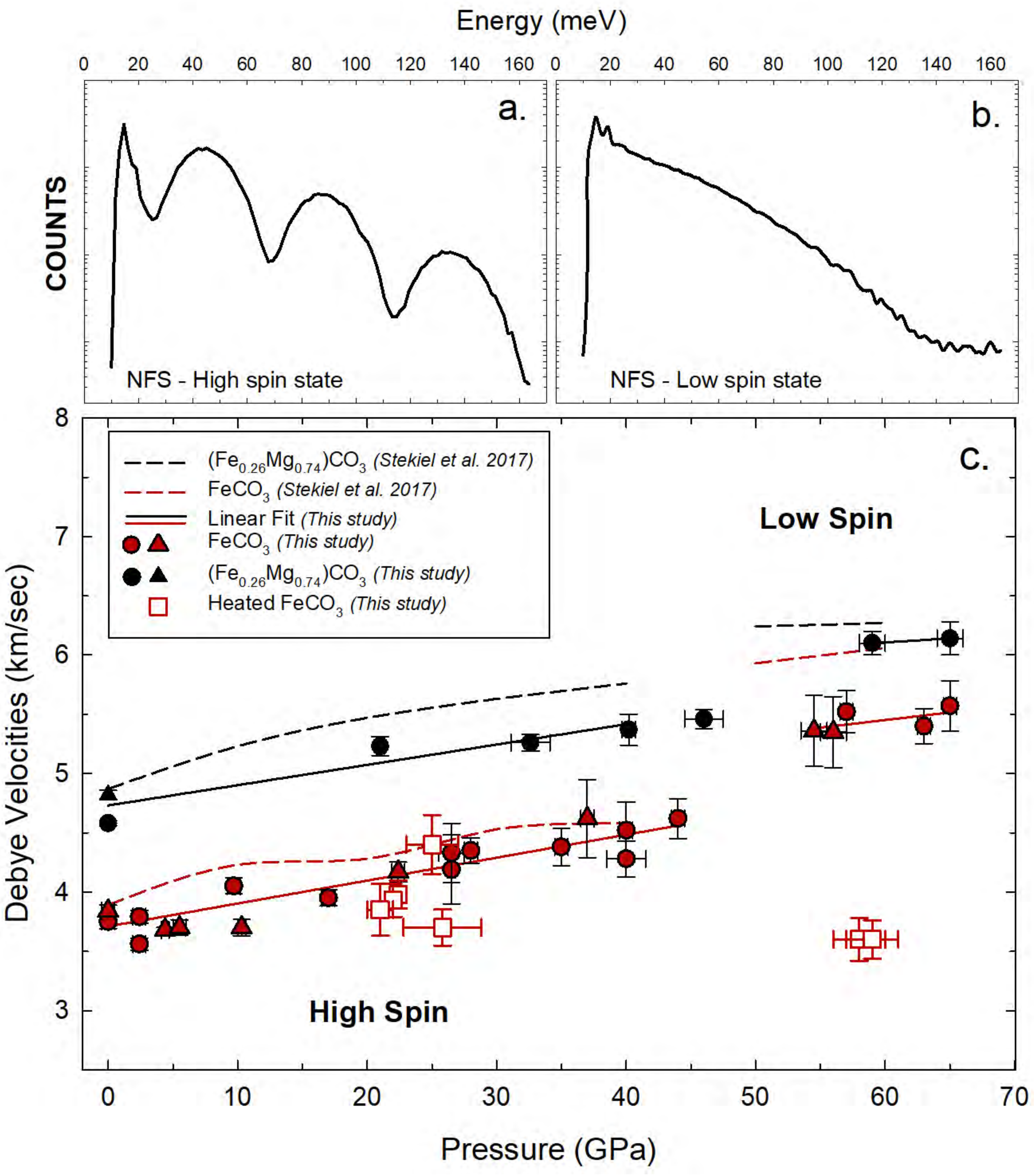
Energy (meV)
0 20 40 60 80 100 120 140 160
a.
NFS - High spin state
b.
NFS - Low spin state
COUNTS
C.
Low Spin
High Spin
(Fe0.26Mg0.74)CO3 (Stekiel et al. 2017)
FeCO3 (Stekiel et al. 2017)
Linear Fit (This study)
FeCO3 (This study)
(Fe0.26Mg0.74)CO3 (This study)
Heated FeCO3 (This study)
Debye Velocities (km/sec)
3 4 5 6 7 8
0 10 20 30 40 50 60 70
Pressure (GPa)

Figure 4

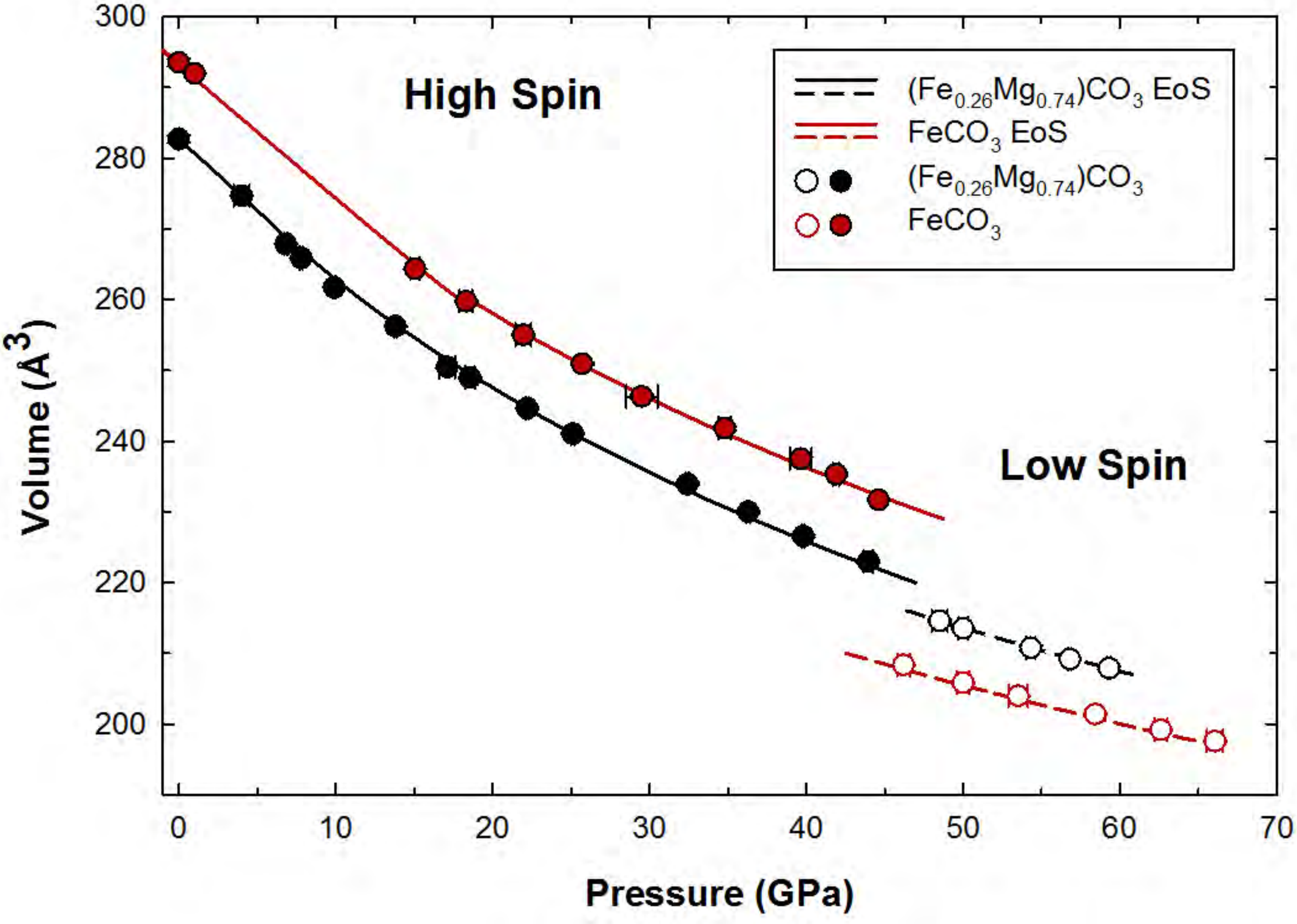
High Spin
Low Spin
(Fe0.26Mg0.74)CO3 EoS
FeCO3 EoS
(Fe0.26Mg0.74)CO3
FeCO3
Volume (Å3)
Pressure (GPa)
300
280
260
240
220
200
0
10
20
30
40
50
60
70

Figure 5a

Figure 5b

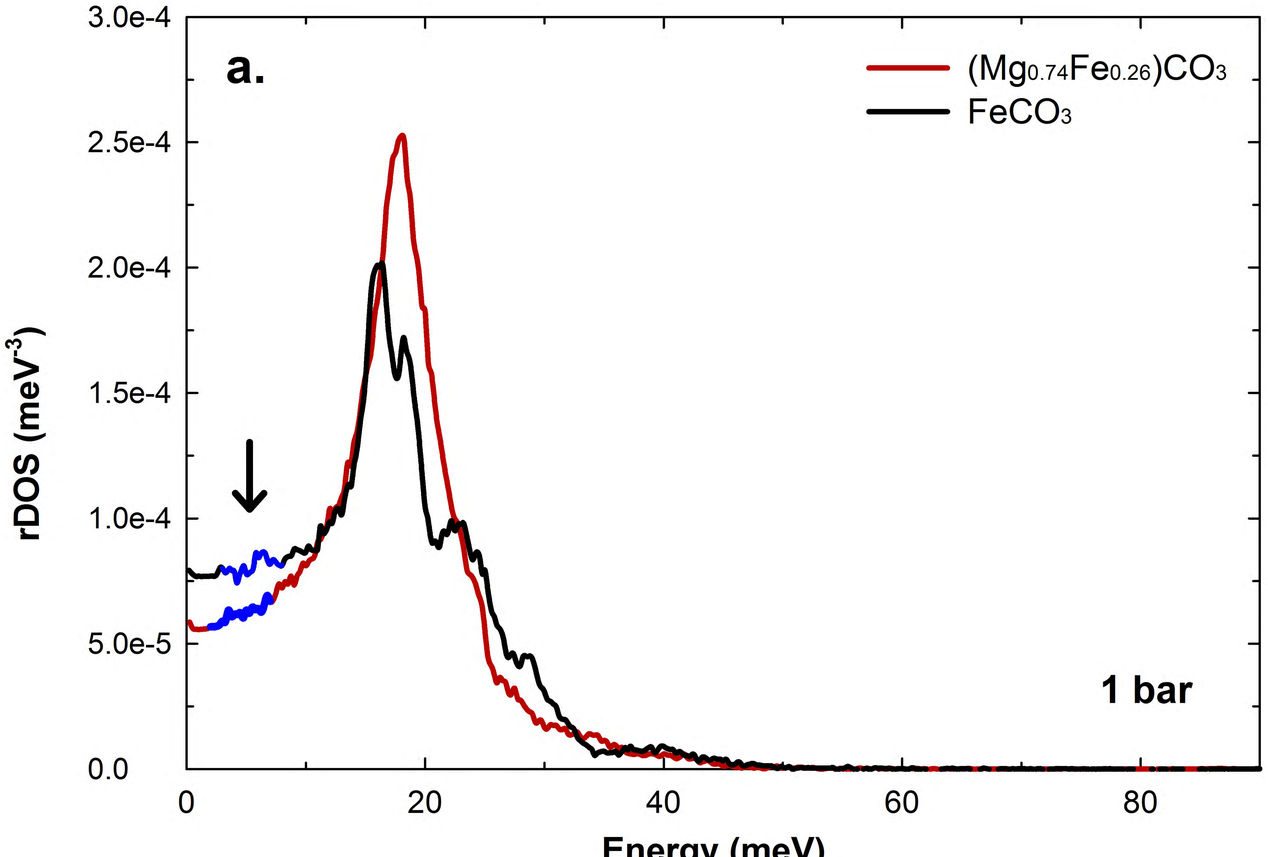

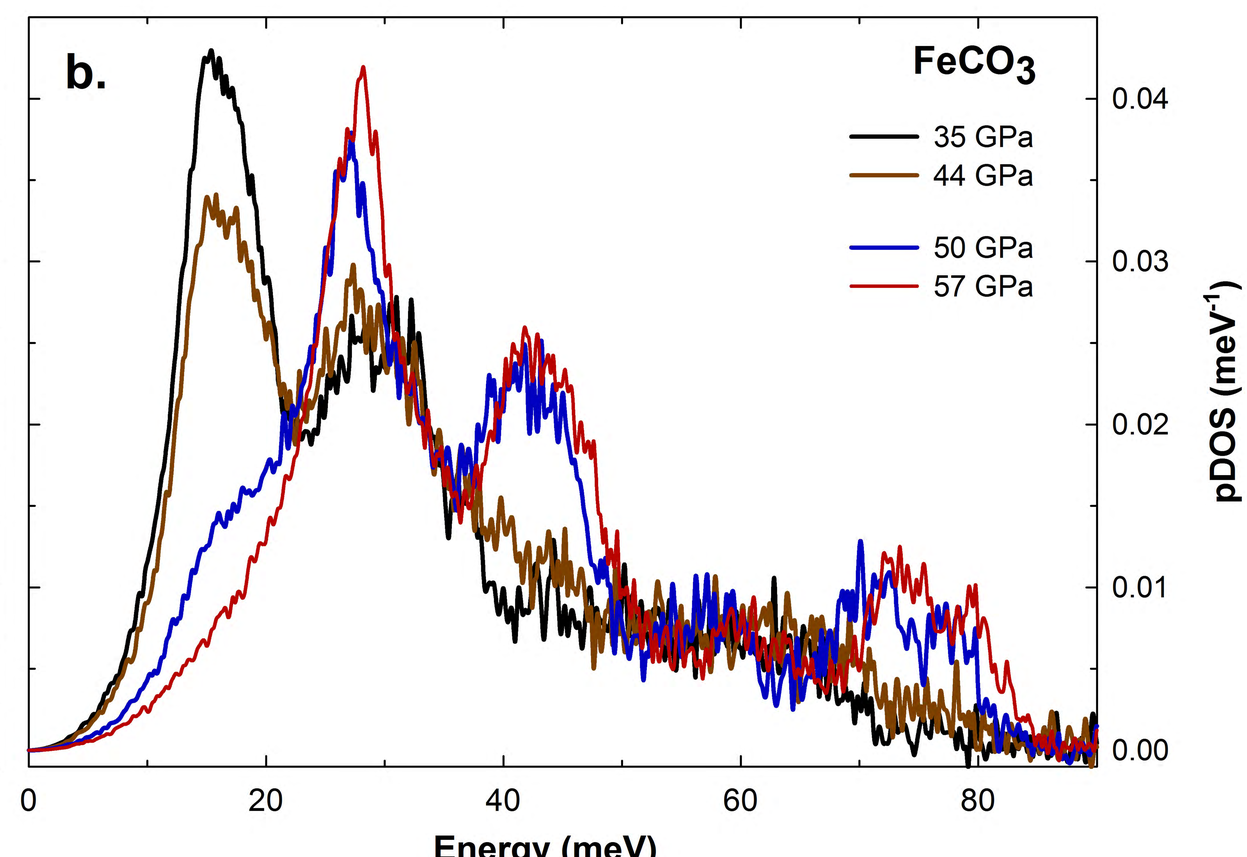

Figure 6

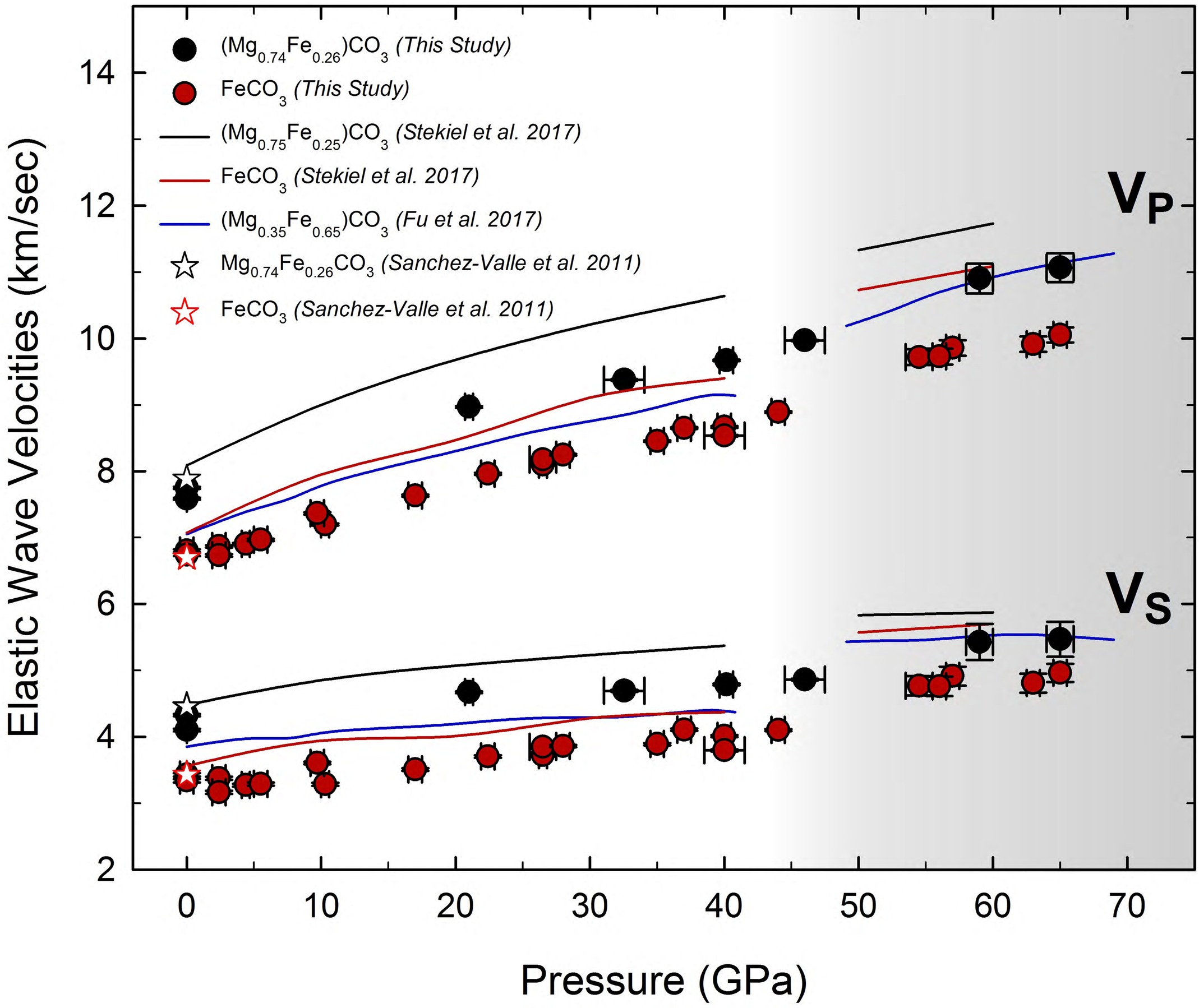
(Mg0.74Fe0.26)CO3 (This Study)
FeCO3 (This Study)
(Mg0.75Fe0.25)CO3 (Stekiel et al. 2017)
FeCO3 (Stekiel et al. 2017)
(Mg0.35Fe0.65)CO3 (Fu et al. 2017)
Mg0.74Fe0.26CO3 (Sanchez-Valle et al. 2011)
FeCO3 (Sanchez-Valle et al. 2011)
VP
VS
Elastic Wave Velocities (km/sec)
Pressure (GPa)
2
4
6
8
10
12
14
0
10
20
30
40
50
60
70

Figure 7

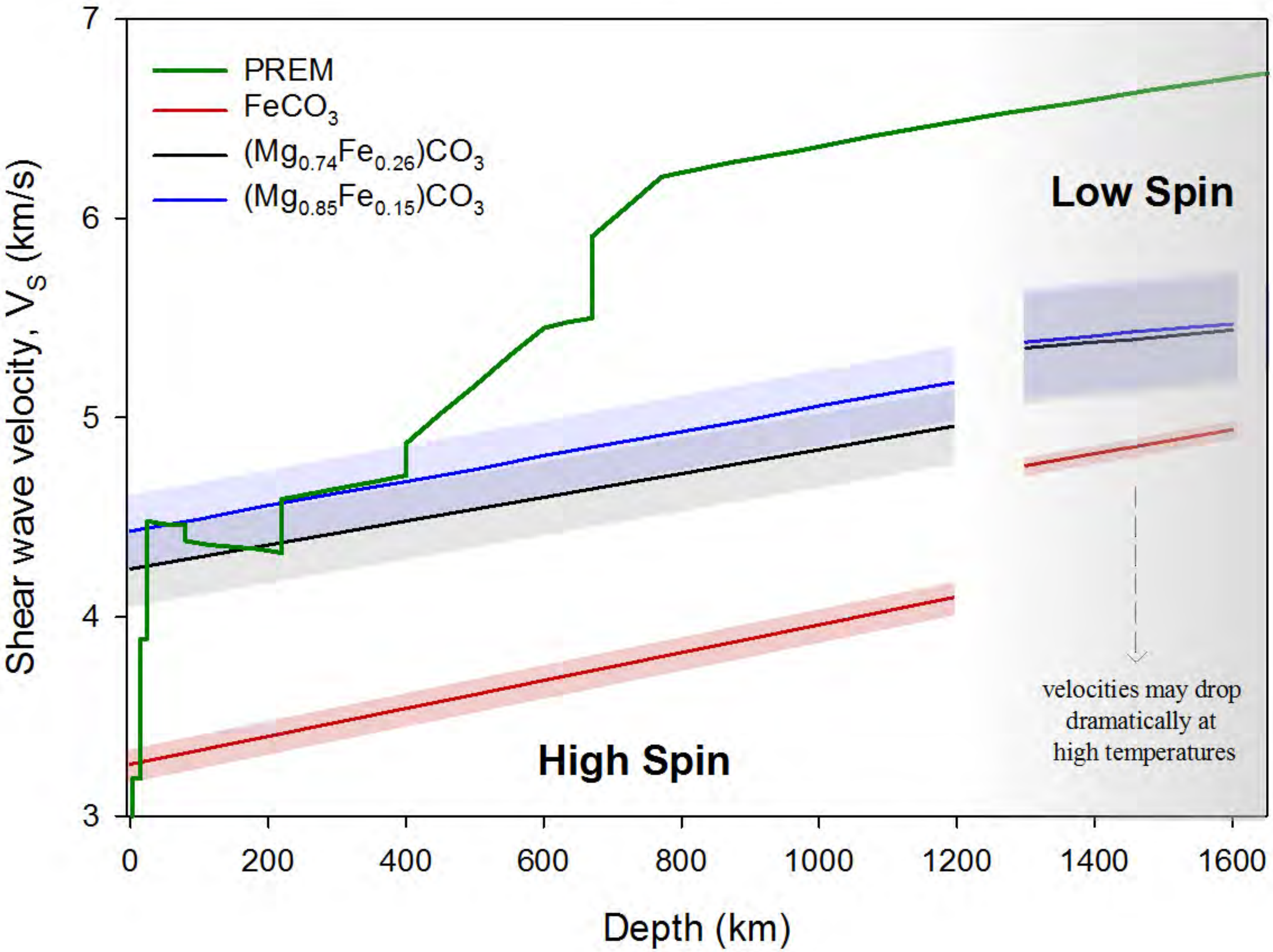
PREM
FeCO3
(Mg0.74Fe0.26)CO3
(Mg0.85Fe0.15)CO3
Low Spin
High Spin
velocities may drop dramatically at high temperatures
Shear wave velocity, VS (km/s)
Depth (km)
7
6
5
4
3
0
200
400
600
800
1000
1200
1400
1600